A large aperture magnification lens for velocity map imaging

Yongwei Zhang,[1,2] Chung-Hsin Yang,[1] Shiou-Min Wu,[1] Andre van Roij,[1]
Wim J. van der Zande,[1] David H. Parker,[1,a)] and Xueming Yang[2]
[1]*Radboud University Nijmegen, Institute for Molecules and Materials, Heijendaalseweg 135, 6525 ED Nijmegen, The Netherlands*
[2]*State Key Laboratory of Molecular Reaction Dynamics, Dalian Institute of Chemical Physics, Chinese Academy of Sciences, 457 Zhongshan Road, Dalian 116023, China*

(Received 16 July 2010; accepted 4 October 2010; published online 13 January 2011)

We have designed and implemented a large aperture electrostatic Einzel lens that magnifies the images of low energy ions or electrons in a standard velocity map imaging apparatus by up to a factor of 5 while allowing the normal use of the apparatus (without blocking any part of the detector). The field strength in the interaction region remains reasonably constant with or without magnification, and the lens can be used in the normal "crush" mode or with any of the different variants of the "slicing" mode. We have characterized the performance of the lens by imaging ion recoil due to two-photon resonant three-photon ionization [(2+1) REMPI] of O($^3P_2$) atoms and by imaging slow NO molecules from the near-threshold photodissociation of the NO–Ar van der Waals complex. © *2011 American Institute of Physics*. [doi:10.1063/1.3505491]

I. INTRODUCTION

In the past decade the ion imaging technique[1] and its high resolution variant velocity map imaging[2] have become increasingly popular for the study of photodissociation, photoionization, and crossed-beam scattering processes.[3] In a velocity map imaging apparatus an electrostatic immersion lens projects ions or electrons created at the crossing point of a laser and a molecular beam toward a two-dimensional (2D) detector, which usually consists of a pair of microchannel plates (MCPs) followed by a phosphor screen and a camera system to record the positions of impact of the particles on the detector surface. Ions with zero nascent velocity perpendicular to the projection direction arrive at a single point on the detector, and the distance from this zero point to any other impact position is directly proportional to the transverse velocity of the particle with respect to the time-of-flight (TOF) direction. Particle mass selection is achieved by increasing the detector gain at the appropriate arrival time. Cylindrical symmetry is maintained in the image by setting the linear polarization of the laser field parallel to the detector face. This allows reconstruction[4] of the 2D image back to the full 3D image using an inverse Abel transformation, or, alternatively, the equivalent information is directly obtained by experimentally detecting only the central "slice" of the incoming ion image.[5–7]

Under velocity mapping conditions all ions or electrons with the same nascent velocity are projected by the immersion lens to the same position onto the detector, independent of where they were formed in the ionization volume, which significantly improves the velocity resolution of the ion imaging experiment. Numerous further improvements of the imaging approach have been reported, including on-the-fly event centroiding,[8] improved velocity map lens shaping,[9] and several different forms of experimental slicing of the image.[10] These improvements in combination with the use of threshold ionization to remove the ion-recoil problem have resulted in the velocity resolution reaching the current level of $\Delta v/v < 0.2\%$.[11]

Another notable improvement in imaging capability was the introduction of a postacceleration zoom lens by Offerhaus and co-workers[12] for magnification of the size of very low velocity images at the detector by up to a factor of 20. For the standard velocity mapping lens geometry the image size is determined by $(\mathrm{KE}/qV_R)^{1/2}$, where KE is the particle kinetic energy release, V_R is the magnitude of the voltage applied to the repeller plate, and q is the particle charge. For a given nascent particle, the repeller plate voltage V_R is used to adjust the size of the image at the detector. As pointed out in Ref. 12, some experiments such as the study of tunneling ionization or Stark effect measurements require keeping V_R fixed at a high value. Even when V_R may be varied, for small images one cannot simply continue lowering the repeller voltage to obtain a desired image size because V_R also determines the kinetic energy of the particles striking the detector surface. The gain of an MCP detector increases nonlinearly with V_R until reaching a saturation plateau above ~1000 V.[13] The rapid decrease of sensitivity at low V_R values thus imposes a practical lower limit of V_R at ~550 V. Typical gain versus voltage characteristics for a dual channelplate show a factor of ~200 loss in gain at 650 V compared to 1100 V.[13] This problem can be avoided by postaccelerating the ions at the end of the TOF tube just before they reach the detector but this usually involves the addition of a grid, which can lower the image quality. Another option is to keep V_R constant at ≥1000 V and increase the TOF distance, as the image size increases linearly with the length of the flight tube. A typical length of a TOF tube used for velocity map imaging is 0.5 m; thus, a factor of 4 in magnification of the image size requires an unwieldy 2 m flight tube.

In the design in Ref. 12 the magnification lens is located in the flight tube region, after the final (ground) electrode

a)Electronic mail:parker@science.ru.nl.

of the imaging lens. The repeller voltage can be kept constant at a desired (high) value, and the image size is adjustable using this additional magnification lens. It should be pointed out that the two main variants of the dc slicing technique introduced independently by Lin and co-workers[7] and by Townsend and co-workers[6] use extra electrodes in the velocity mapping lens region in order to stretch out the region of acceleration. This yields velocity mapping without "pancaking" where the ion packet arrives at the detector over an extended period of time. The center slice of the Newton sphere can be separately detected in this way by using a short pulse on the MCP gain at the appropriate time. These extra lenses in the acceleration region can also be used to magnify the image size, according to Ref. 7 by up to a factor of 5. Magnification and slicing are coupled, however, in this approach. In the magnification lens design presented in this paper, velocity mapping is retained independent of the degree of slicing, as in the approach of Ref. 12.

A drawback of the magnification lens design of Ref. 12 is that half of the detector radius (75% of the area) is blocked when the lens is not in use. The zoom lens must thus be removed for normal operating conditions. Our goal was to design a postacceleration lens which does not block the detector and thus does not have to be removed when not in use. The resulting maximum magnification we achieve in our design is typically a factor of 4–5. For very low velocity particles and thus very small images where our detector spatial resolution ($\sim$40 μ) becomes a limiting factor, the 3-plate Einzel lens of Ref. 12 with its larger magnification range is more suitable.

II. LENS DESIGN

As in the design of Ref. 12, we use an Einzel configuration of three electrodes, with the center lens at a voltage $V_{mag} < V_{rep}$ and the two outer lenses at ground. Maximum magnification (and maximum sensitivity to misalignment) occurs as V_{mag} approaches V_{rep}. Magnification requires that the ion trajectories are first focused by the imaging lens through a point within or near the magnification lens assembly, which should thus be located at least one fourth of the TOF length downstream from the velocity map imaging lens assembly. The largest magnification is achieved with a small lens aperture and a short distance between the inner and outer plates. This small lens aperture, combined with the significant downstream distance, leads to a partial blocking of the detector. Our challenge is thus to design a lens setup with larger lens openings, positioned at a similar downstream position as the 3-plate lens of Ref 12.

Results from a series of ion trajectory simulations suggested changing the shape of the middle lens from a flat plate to a thick (cylindrically symmetric) hyperbolic lens whose shape is shown in Fig. 1, which mimics the form of the fields lines created inside the 3-plate lens of Ref. 12. Our thick center lens allows a longer interaction time for the ions as they pass through the magnification lens, and the shape of the center lens allows linear magnification when using a larger (15 mm compared to 10 mm for the 3-plate lens) aperture. The inner and outer lenses are thin flat plates, also with

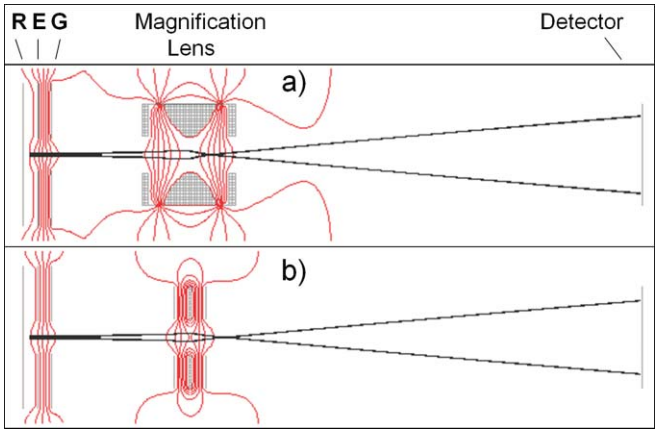

FIG. 1. (Color online) [SIMION software (Ref. 14)] (a) Potential fields for the present design with a 1300 V repeller, 1076 V extractor, and 1142 V magnification lens (center lens in the figure). (b) Potential fields for the standard 3-plate Einzel lens with 1300 V repeller, 1080 V extractor, and 1256 V on the center plate of the Einzel lens.

15 mm apertures. This allows the use of a detector with up to 60 mm diameter without reducing the field of view.

As we confirm below, electrostatic lens design usually requires that ions remain within the center 10% of the lens opening in order to avoid distortions. An electrostatic (magnification) lens placed one fourth of the way downstream in the flight tube with a 40 mm detector then requires a lens opening diameter of 10 $\times$ 10 mm = 100 mm when the detector is filled. When using a magnification factor of 3 and thereby obtaining a full 40 mm diameter image, the lens opening should thus be at least 33 mm. We must evaluate the resulting distortion when using a 15 mm opening, which could result in a nonlinear magnification as a function of radius. Ion trajectory simulations, shown in Fig. 2, indicate that with the special

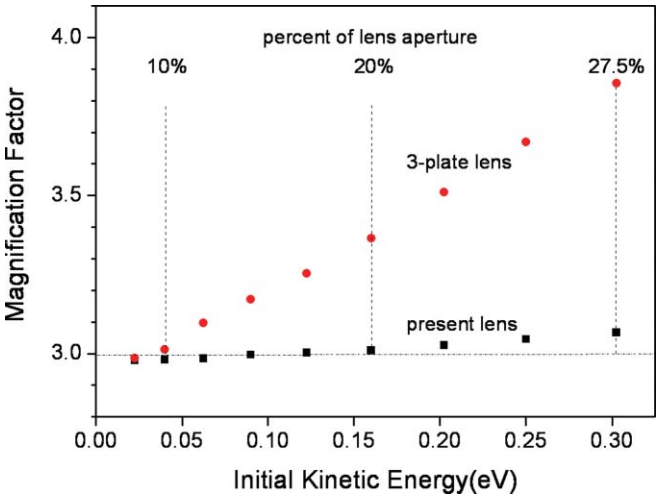

FIG. 2. (Color online) Comparison of the calculated magnification factor of the present lens design with that of the standard three flat plate design as a function of initial kinetic energy of a NO^+ ion using SIMION simulation. A kinetic energy of 0.04 eV corresponds to an ion trajectory passing at a radius of 1.5 mm or at 10% of our lens opening. Ions with higher kinetic energy than this enter regions of the standard 3-plate lens where the magnification factor is not constant, while in our design the magnification factor remains reasonably constant up to kinetic energies of 0.30 eV, corresponding to a radius of 4.2 mm or 27.5% of the lens opening.

shape of the center electrode in our magnification lens, the magnification parameter remains reasonably constant when using up to 27% of the lens opening while the 3-plate design shows the expected deviations when more than 10% of the opening is used.

The mapping lens assembly at the laser ionization interaction region (repeller, extractor, and the front of the TOF tube) and the magnification lens can be adjusted separately by a high voltage supply. In practice, for a given V_{rep} the extractor voltage is adjusted to yield a sharp image with $V_{mag} = 0$. V_{mag} is then set to a fixed voltage below V_{rep} and then the extractor voltage is adjusted slightly to obtain a sharp image. (Typically we use 1300 V on the repeller, 1070 V on the extractor, and 1142 V on the inner electrode of the magnification lens.) For convenience this adjustment should be done first with a strong signal. As long as the position of the ionization laser remains fixed, the optimal values for V_{ext} and V_{mag} remain constant for a given V_{rep}. Distortions of the image are observed, as in the design of Ref. 12, when large diameter images are recorded using the largest magnification settings. Misalignment of the neutral molecular beam axis with the velocity map lens axis and the center of the magnification lens is the main cause of these distortions.

III. EXPERIMENTAL APPLICATIONS

A. Ion recoil from (2+1) REMPI of O(^{3}P$_2$) atoms at 226 nm

Our first example of the utility of the magnification lens compares imaging of a fast, e.g., 3500 m/s (1.0 eV) O atom, versus a slow 35 m/s (0.1 meV) O atom, with the speed (meter per second) referring to the detector plane, perpendicular to the time-of-flight axis. Fast O atoms can be created, e.g., by photodissociation of O_2, while slow atoms are created in the present example from a discharge in an O_2 nozzle, which produces primarily O(^{3}P$_2$) atoms that are cooled in the ensuing supersonic expansion. (2+1) REMPI at 226 nm is then used to detect the O(^{3}P$_2$) atoms. The energy sum of three 226 nm photons is 2 eV higher than the O atom ionization potential, whereby 35 m/s recoil is imparted to the O atom by the ejected 2 eV photoelectron. A convenient repeller voltage for our apparatus of $V_R = 3000$ V projects a 3500 m/s particle to a distance 10 mm from the center of the detector while the 35 m/s particle arrives 100 μm from the detector center. This small size approaches with the spatial resolution limit ($\sim$40 μm) of our MCP detector assembly. Imaging the ring created by the 35 m/s particle will thus not be practical under these conditions. One could lower the repeller voltage to the lower limit of $\sim$550 V (loss in gain $\sim$1000). Because the image size is proportional to $(V_{rep})^{-1/2}$, this will double the image radius to 200 μm, which is still quite small. The magnification factor of 5 by our lens provides a 1 mm diameter image of zero nascent velocity, ion-recoiled O^+ atoms shown in Fig. 3. The angular distribution is characterized by

$$I(\theta) = (1/4\pi)\,[1 + \beta P_2(\cos\theta)]\,,$$

where $P_2(\cos\theta)$ is the second Legendre polynomial and θ is the angle between the fragment recoil direction and the polarization direction. The normalization factor $1/4\pi$ corresponds to unit probability for the integral of $I(\theta)$ over all solid angles. A value of $\beta = +2$ corresponds to ionization of a pure s electron, yielding a p electron wave, while a value of $\beta = -1$ corresponds, for example, to ionization of a p electron with perfect interference of the outgoing s and d waves. The ion-recoil image of Fig. 2 yields a negative beta parameter ($\beta \sim -0.2$) similar to the negative beta parameter Cooper and Zare found for the photodetachment of O^-,[15] In both cases a $2p$ electron is ejected but the similarity in beta is most likely a simple coincidence. More importantly, this beta information can be used to understand image distortion due to ion recoil. This recoil velocity is added to each velocity point of any nascent particle image[16] and can significantly lower the image resolution. For velocity map imaging applications the O(^{3}P) atom ion recoil has a maximum effect on perpendicular photodissociation processes, as was recently shown for the direct dissociation of OH by excitation of the repulsive $^2\Sigma^-$ state from the $^2\Pi$ ground electronic state.[17]

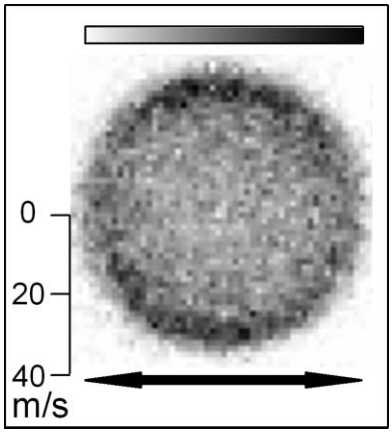

FIG. 3. O^+ image from a beam of cold O(^{3}P$_2$) atoms formed in a discharge and ionized by (2 + 1) REMPI at 226 nm. Darker areas correspond to higher signal. The arrow marks the direction of the laser polarization. Recoil due to the REMPI process is maximal in the direction perpendicular to the laser polarization and characterized by $\beta = -0.2$. Note that the CCD pixel resolution exceeds the imaging detector resolution in this image.

B. Photodissociation of Ar–NO clusters at 224.7 nm

The photodissociation of Ar–NO clusters[18] around $h\nu = 224.7$ nm,

$$\mathrm{Ar-NO}\left(\tilde{X}^2\Pi\right) + h\nu \rightarrow \mathrm{Ar} + \mathrm{NO}\,(\tilde{A}, \mathrm{N}),$$

where N is the rotational angular momentum quantum number of NO in the $\tilde{A}^2\Sigma$ electronic state, is used as our second example to evaluate the performance of the magnification lens. This is a convenient test system because it provides a series of easily ionized, low velocity NO $\tilde{A}$ state fragments. In order to improve the image resolution compared to the original article[18] describing this system, we used (1 + 1′) REMPI at (224.7 + 295 nm) where the second, lower energy, photon causes less ion recoil (5 m/s compared to 16 m/s with (1 + 1) REMPI at $\sim$226 nm.

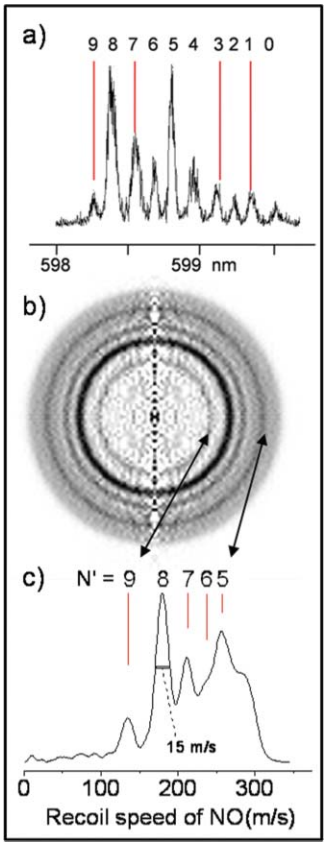

FIG. 4. (Color online) (a) (1 + 1) REMPI spectrum of NO($\tilde{A}$,N) products from the photodissociation of Ar–NO($\tilde{X}$) at 224.70 nm. (b) NO^+ image taken using the same dissociation laser as in (a) but with direct one-photon ionization of all NO($\tilde{A}$,N) products using 295 nm. Polarization and intensity scale information as in Fig. 3. (c) Velocity distribution of the image in (b) taken with the magnification lens set at 1142 V, for comparison with the spectrum shown in panel (a).

Ground state Ar–NO($\tilde{X}$, $v = 0$) van der Waals clusters were prepared in a pulsed supersonic expansion of 10% NO in Ar with a backing pressure $P_0 = 1.5$ bar. The mixture was expanded at 10 Hz from a pulsed valve with a nozzle diameter of 1.0 mm. The molecular beam passes through a 2.0 mm hole in the repeller plate and is crossed by a laser beam tuned to 224.70 nm with a linear polarization aligned parallel to the detector face.

Three experiments were performed at a dissociation laser wavelength of 224.70 nm; (a) a (1+1) REMPI spectrum that provides the total yield of individual NO($\tilde{A}$,N) products, (b) a single magnified image where all NO($\tilde{A}$,N) products are detected simultaneously by direct one-photon ionization, and (c) images of single N-state products using (1 + 1) REMPI tuned to individual N-state resonances. Comparison of the different datasets provides information on the resolution limiting steps in obtaining the magnified images.

(a) This first laser causes photodissociation of $Ar - NO(\tilde{X}, v = 0)$ to Ar and NO($\tilde{A}$, $v = 0$, N) and the ionization laser is tuned from 598–599.7 nm in order to cause (1 + 1) ionization of $N' = 0, 1, 2, \ldots, 9$ of NO($\tilde{A}$, $v' = 0$, N) via the $E^2\Sigma^+(v = 0)$ state, as was used in a similar manner in Ref. 18. The total ion signal collected on the imaging detector as a function of wavelength is shown in Fig. 4(a). At this dissociation wavelength, corresponding to an energy of 230 cm^{-1} above the barrier to cluster dissociation, two product peaks, N = 8 and N = 5 are significantly enhanced compared to the other N states. This two peak maximum behavior has been characterized as a rotational rainbow effect in previous study by Sato *et al.*[19] Yields of the individual N states are evident in this spectrum.

(b) In panel (b) of Fig. 4 an image of NO^+ ions is shown from the ionization of NO ($\tilde{A}$, $v' = 0$,N) created by photodissociation of Ar–NO at 224.70 nm. The corresponding voltages on the repeller and extractor electrodes are 1300 and 974 V, respectively, without the zoom lens on and 1300 and 1019 V with the magnification lens at 1142 V voltage, which gave a magnification factor of ~3. The second (ionization laser) was fixed at 295 nm which is 3029 cm^{-1} above the ionization threshold of NO. The ion-recoil velocity is ~5 m/s, which leads to a minimal peak width of 10 m/s. Further broadening of a single peak will arise from the geometric velocity spread (2 mm collimator 100 mm downstream of 0.5 mm nozzle with 650 m/s beam velocity gives >7 m/s broadening) and the spread in internal energy of the Ar–NO cluster. The measured full-width at half maximum from peak N = 8 in Fig. 4(b) is ~15 m/s. Panel (c) of Fig. 4 shows the velocity distribution of the image shown in panel (b). As in panel (a), the N = 8 and N = 5 peaks are prominent in the image.

(c) Images taken for individual NO($\tilde{A}$,N) molecules using (1 + 1) REMPI tuned to peaks shown in Fig. 4(a) are shown as insets in Fig. 5(a) with the magnification lens voltage at 0 V and in Fig. 5(b) with the lens voltage at 1200 V. Under these conditions the magnification factor was measured for each value of N, as plotted in Fig. 5. An average value of 3.98 ± 0.04 was found, with the scatter in values determined mainly by noise in the images. The slope of a line through the magnification values is zero within the range of uncertainty.

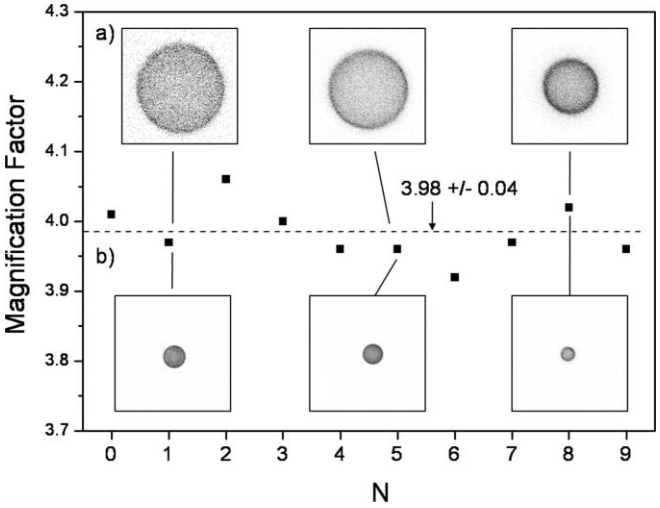

FIG. 5. Insets in (a) show NO^+ images obtained for individual rotational states of NO ($\tilde{A}$, $v' = 0$, N) with the magnification lens at 1200 V, and in (b) with the magnification lens at 0 V. Also shown are the measured magnification values for each separate N state.

IV. DISCUSSION AND CONCLUSION

A large aperture electrostatic Einzel lens that magnifies the images of low energy ions or electrons in a standard velocity map imaging apparatus by up to a factor of 5 is described. The special thick hyperbolic shape of the center electrode was shown to allow use of more than the standard 10% of the open aperture of the lens assembly. The most important feature is that the magnification lens allows the normal operation of the apparatus (without blocking any part of the detector) when it is not in use. Because it is positioned in the postacceleration part of the apparatus, the field strength in the laser interaction region remains reasonably constant with or without magnification, and the lens can be used in the normal "crush" mode or with any of the different variants of the "slicing" mode. We have characterized the performance of the lens by imaging ion recoil due to two-photon resonant three-photon ionization [(2+1) REMPI] of $O(^3P_2)$ atoms. A beta parameter for the measured angular distribution of −0.2 was determined. We note that a similar beta parameter was found for the corresponding photoelectrons, but that it was not possible in this study to obtain a distortion free photoelectron image in the test apparatus due to the presence of magnetized components near the flight tube. This also implies that ion-recoil measurements when combined with a magnification lens could be a convenient alternative to photoelectron imaging when using a general purpose imaging apparatus. In a second test example, slow NO molecules formed from the near-threshold photodissociation of the NO–Ar van der Waals complex were measured. The Einzel lens yielded the same value of magnification for a wide range of NO product states, and the resolution of the images was shown to be affected by ion recoil, geometric velocity spreading, and internal energy in the parent van der Waals complex. We also note that while the magnification lens causes all ions to pass through a focus point downstream of the lens (see Fig. 1), we do not see evidence in Fig. 5 of a decrease in image resolution due to space charge effects at this focal point. The images shown in Fig. 5 were taken at a low ion formation rate (∼10 ions/laser shot); a higher formation rate could lead to broadening of the image features.

ACKNOWLEDGMENTS

The authors gratefully acknowledge support from the Radboud University, EU Molecular Universe network and from the Chinese Academy of Sciences for this project.

[1] D. W. Chandler and P. L. Houston, J. Chem. Phys. **87**, 1445 (1987).
[2] A. T. J. B. Eppink and D. H. Parker, Rev. Sci. Instrum. **68**, 3477 (1997).
[3] M. N. R. Ashfold, N. H. Nahler, A. J. Orr-Ewing, O. P. J. Vieuxmaire, R. L. Toomes, T. N. Kitsopoulos, I. A. Garcia, D. A. Chestakov, S. M. Wu, and D. H. Parker, Phys. Chem. Chem. Phys. **8**, 26 (2006).
[4] A. T. J. B. Eppink, S. M. Wu, and B. J. Whitaker, "Reconstruction methods," in *Imaging in Molecular Dynamics* (Cambridge University Press, Cambridge, 2003).
[5] C. R. Gebhardt, T. P. Rakitzis, P. C. Samartzis, V. Ladopoulos, and T. N. kitsopoulos, Rev. Sci. Instrum. **72**, 3848 (2001).
[6] D. Townsend, M. P. Minitti, and A. G. Suits, Rev. Sci. Instrum. **74**, 2530 (2003).
[7] J. J. Lin, J. G. Zhou, W. C. Shiu, and K. P. Liu, Rev. Sci. Instrum. **74**, 2495 (2003).
[8] B. Y. Chang, R. C. Hoetzlein, J. A. Mueller, J. D. Geiser, and P. L. Houston, Rev. Sci. Instrum. **69**, 1665 (1998).
[9] E. Wrede, S. Laubach, S. Schulenburg, A. Brown, E. R. Wouters, A. J. Orr-Ewing, and M. N. R. Ashfold, J. Chem. Phys. **114**, 2629 (2001).
[10] D. A. Chestakov, S. M. Wu, G. R. Wu, D. H. Parker, A. T. J. B. Eppink, and T. N. Kitsopoulos, J. Phys. Chem. A **108**, 8100 (2004).
[11] M. L. Lipciuc, J. B. Buijs, and M. H. M. Janssen, Phys. Chem. Chem. Phys. **8**, 219 (2006).
[12] H. L. Offerhaus, C. Nicole, F. Lepine, C. Bordas, F. Rosca-Pruna, and M. J. J. Vrakking, Rev. Sci. Instrum. **72**, 3245 (2001).
[13] J. L. Wiza, Nucl. Instrum. Methods **162** (1979).
[14] A. V. Crewe, Optik (Stuttgart) **90**, 151 (1992).
[15] J. Cooper and R. N. Zare, J. Chem. Phys. **48**, 942 (1968).
[16] D. H. Parker, R. F. Delmdahl, B. B. L. G. Bakker, and H. P. Loock, J. Chin. Chem. Soc. **48**, 327 (2001).
[17] D. Č. Radenović, A. J. A. van Roij, S. M. Wu, J. J. Ter Meulen, D. H. Parker, M. P. J. van der Loo, L. M. C. Janssen, and G. C. Groenenboom, Mol. Phys. **106**, 557 (2008).
[18] B. F. Parsons, D. W. Chandler, E. C. Sklute, S. L. Li, and E. A. Wade, J. Phys. Chem. A **108**, 9742 (2004).
[19] K. Sato, Y. Achiba, H. Nakamura, and K. Kimura, J. Chem. Phys. **85**, 1418 (1986).